Journal of Physics and Chemistry of Solids 74 (2013) 1341–1348

Contents lists available at SciVerse ScienceDirect

Journal of Physics and Chemistry of Solids

journal homepage: www.elsevier.com/locate/jpcs

Review

Experimental Compton profiles of Be, Al and Ti and comparisons to generalized gradient approximation calculations

Julio C. Aguiar [a,b,*], Héctor O. Di Rocco [b,c], Darío Mitnik [c,d]

[a] Autoridad Regulatoria Nuclear, Av. Del Libertador 8250, (C1429BNP) Buenos Aires, Argentina
[b] Instituto de Física "Arroyo Seco", Facultad de Ciencias Exactas, Universidad Nacional del Centro de la Provincia de Buenos Aires, Pinto 399, 7000 Tandil, Argentina
[c] Consejo Nacional de Investigaciones Científicas y Técnicas (CONICET), Argentina
[d] Instituto de Astronomía y Física del Espacio (IAFE), C.C. 67, Suc. 28, (C1428EGA), Buenos Aires, Argentina

ARTICLE INFO

Article history:
Received 12 July 2012
Received in revised form
22 March 2013
Accepted 25 April 2013
Available online 23 May 2013

Keywords:
A. Electronic materials
C. Ab initio calculations
D. Electronic structure

ABSTRACT

Experimental analysis of isotropic Compton profiles for beryllium, aluminum and titanium was performed to assess the radial core wavefunctions and pseudo-orbitals for valence electrons generated using a generalized gradient approximation based on norm-conserving pseudo-potential calculations. Compton profiles for the different core and valence electron shells are presented in tabulated electron momentum transfer values from $q=0$ to 9 a.u. Derivatives of the Compton profiles were also calculated to identify the Fermi momenta. Comparison of our results to previous experimental and theoretical calculations shows acceptable agreement in most cases. Our findings indicate that the Compton profiles for Be, Al and Ti are reasonably well described within the generalized gradient approximation.

Contents

1. Introduction

The inelastic scattering of X-rays and γ-rays by electrons (Compton scattering) is intrinsically linked to electron density distributions. There is a strong relationship between the motion of the target electrons and line-broadening of the Compton spectrum. This Doppler-broadened line shape is known as the Compton profile (CP) [1,2]. CP analysis is widely used as a tool to extract information about the electronic structure of a target system, with several applications in atomic and molecular physics, condensed matter physics and materials science [3]. Since the information acquired resides in momentum space, it can complement that obtained from other standard techniques such as positron annihilation. Since the position and momentum distributions are related by Fourier transforms, each electron orbital contributes to the CP in a quite different way according to its spatial localization. Consequently, the outermost valence electrons, which have largely spread orbitals over the radial space, are highly localized in momentum space and therefore contribute to CP with sharp peaks. By contrast, the inner electrons have spatial orbits circumscribed by small distances and produce broad lines that are generally spread out to high momenta in CPs.

* Corresponding author at: Autoridad Regulatoria Nuclear, Av. Del Libertador 8250, (C1429BNP) Buenos Aires, Argentina. Tel.: +54 11 6323 1370; fax: +54 11 6323 1375.
E-mail addresses: jaguiar@arn.gob.ar, jcaguiar74@hotmail.com (J.C. Aguiar).

0022-3697/$ - see front matter © 2013 Elsevier Ltd. All rights reserved.
http://dx.doi.org/10.1016/j.jpcs.2013.04.018

Many experimental and theoretical studies have examined CPs for different elements and molecules. Our aim here is not to present an exhaustive list of established methods, but rather to mention some experimental and theoretical results for comparison with our findings. Biggs et al. performed Hartree–Fock (HF) calculations for atomic orbital wavefunctions and published a CP data table for all the orbitals of all free atoms up to $Z=102$ [4]. CPs have been largely studied for noble gases. CP experiments on He, Ne, Ar, Kr gases have generally been in very good agreement with HF calculations [5–8].

Density functional theory (DFT) is widely used as a theoretical framework for calculating the electronic structure of solids. Many studies have compared *ab initio* DFT calculations and experimental CP measurements. Sakurai et al. performed synchrotron X-ray experiments to study CPs for He, Ar and Xe and compared them to DFT results [9]. Although DFT methods often give bulk properties that are more accurate than HF results, many recent studies have highlighted the failure of standard Kohn–Sham DFT in reproducing fine aspects of the electron momentum distributions of molecules and crystals. Thakkar and Hart calculated electron momentum densities for many closed-shell molecules and found that DFT methods give relatively poor results for these systems that were often worse than the HF approach [10,11]. Recent comparisons of experimental directional CPs for many crystals and DFT calculations with different exchange-correlation functionals were generally satisfactory [12–15]. However, some disagreement was evident, which demonstrates the inability of standard DFT to describe all correlations correctly.

The local-density approximation (LDA) [16,17] has proved to be remarkably successful in predicting various bulk properties of different solids. LDA is a powerful theoretical tool but it cannot account for nonlocal contributions to exchange-correlation effects. It is known that theoretical CPs obtained by LDA calculations are overestimated at low transfer momenta and underestimated at higher momenta. A widely used method that accounts for the neglected exchange and correlation effects is the Lam–Platzman correction [18–20], which substantially resolves the residual discrepancies outlined above and facilitates a critical assessment of CPs (and their respective derivatives) calculated within the LDA.

An improvement over LDA is the generalized gradient approximation (GGA) [21], which modifies the LDA by adding gradient corrections to the local density model. Different GGA functionals have been successfully tested in calculations of equilibrium lattice constants, bulk moduli, and the cohesive energy of solids [22–24]. Some researchers have reported CPs calculated under the GGA approach and compared them with LDA results [12–15,25–28].

In this study we selected three representative metals with relevant technological applications and belonging to different groups of the periodic table for isotropic CP analysis: beryllium (alkaline earth metal), aluminum (post-transition metal) and titanium (transition metal).

Experimental directional CPs for Be have been reported [29–33] and qualitative agreement with theoretical calculations was obtained. Isotropic CP experiments have also been reported [34,35].

There have been many theoretical and experimental CP investigations for Al [36–39,28] and these have been reviewed and summarized by Berggren [40].

Transition metals are very difficult to treat theoretically. Neither free-atom approximations nor the free electron model has provided accurate descriptions of CPs for Ti. In particular, the low-momentum transfer region, which corresponds to the valence electrons, shows significant deviations from free-atom behavior. Renormalized free-atom (RFA) model calculations are in good agreement with experimental results [41,42]. Further references on CP calculations for this element can be found in [43,44].

The aim of the present study was twofold. First, we were interested in the capability of the functional GGA-PBE theory, proposed by Perdew et al. [21], to describe the momentum-space properties of solids and CPs in particular. The theoretical results published here can be useful in evaluating the necessity of considering additional corrections for the correlation terms. Second, we constructed a low-intensity $\gamma-$ray Compton spectrometer. An additional objective was to evaluate the performance of our device and to compare experimental CPs with our GGA calculations and with other previous results.

The remainder of the paper is organized as follows. Section 2 outlines the main equations and the computational procedures used in the calculations. Section 3 describes the experimental setup. The results are presented in Section 4 and conclusions are drawn in Section 5.

2. Theory and computational procedures

We performed theoretical calculations for isotropic CPs of solids within the impulse approximation for one-electron wavefunctions of the form

$$\psi_{nlm}(r,\theta,\phi)=R_{nl}(r)Y_l^m(\theta,\phi). \tag{1}$$

The radial wavefunction $R_{nl}(r)$ is Fourier transformed according to

$$\chi_{nl}(p)=\left(\frac{2}{\pi}\right)^{1/2}(-i)^l\int_0^\infty R_{nl}(r)j_l(p\,r)r^2\,dr, \tag{2}$$

where $j_l(pr)$ is the spherical Bessel function of the first type and p is the electron momentum in the atom [45]. CP $J_{nl}(q)$ for the nl orbital is defined as

$$J_{nl}(q)=\frac{1}{2}\int_{|q|}^\infty \frac{I_{nl}(p)}{p}\,dp, \tag{3}$$

where $I_{nl}(p)$ is defined in terms of the electron momentum density $\chi_{nl}(p)$ as

$$I_{nl}(p)=|\chi_{nl}(p)|^2p^2 \tag{4}$$

and q is the projection of the momentum transfer $\mathbf{k}$ on the electron momentum $\mathbf{p}$ before collision:

$$q=-\frac{\mathbf{k}.\mathbf{p}}{k}. \tag{5}$$

Our computational procedures are based on the Hohenberg–Kohn variational principle and the self-consistent Kohn–Sham equations. The Hohenberg–Kohn theorem [46] states that the energy of a condensed system is a functional of its electronic density $\rho(r)$, and the correct energy density is the one that minimizes the total energy of the system. The Kohn–Sham self-consistent radial single-particle equation is [47]

$$\left(-\frac{1}{2}\frac{\partial^2}{\partial r^2}+\frac{l(l+1)}{2r^2}+V^{sc}[\rho;r]\right)P_{nl}(r)=\varepsilon_{nl}P_{nl}(r), \tag{6}$$

where $P_{nl}(r)\equiv rR_{nl}(r)$ is the reduced radial wavefunction and $V^{sc}[\rho;r]$ is the self-consistent single-particle potential [48]. The electron density is calculated by summing the electron densities of all the occupied states:

$$\rho(r)=\sum_{nl}|R_{nl}(r)|^2. \tag{7}$$

The atomic radial wavefunctions $R_{nl}(r)$ for core electrons, the pseudopotentials (VPS), and the pseudo-atomic orbitals (PAOs) for valence electrons are obtained using the ADPACK code [49]. All VPS and PAOs are generated using Schrödinger–Kohn–Sham nonrelativistic equations under GGA, with a Troullier and Martins (TM) scheme [50]. The norm-conserving pseudopotentials and PAOs generated by this code are used as input data for the OpenMX

program [51] for density functional calculations for molecules and solids [52–55]. Associations between pseudo-wavefunctions and valence electrons in the unit cell of crystalline solids were calculated using OpenMX. Valence orbital calculations were performed using GGA-PBE [21].

All our theoretical calculations for isotropic CPs were performed under the impulse approximation (IA). Limitations to the IA validity in Compton scattering have been widely discussed [56–58]. This approach is expected to be valid when the energy transferred in the scattering process is much greater than the binding energy of the electron orbital. Since the energy transferred in our case is of the order of hundreds of keV, the approximation is suitable.

3. Experimental procedures

We measured CPs for high-purity ($>99.98\%$) Be, Al and Ti of differing thickness (5.0, 1.0 and 0.3 mm) using a mono-energetic ^{137}Cs (661.66 keV) γ source with activity of 1.5×10^{11} Bq (Comisión Nacional de Energía Atómica of Argentina, CNEA). The cylindrical source is 0.53 cm in diameter and 1.84 cm long and is sealed under double encapsulation. The external encapsulation is 1.93 cm in height and 1.28 cm in diameter and is made of type 304 stainless steel.

A high-purity p-type germanium (HPGe) detector (GX6020 model) is used to detect $\gamma-$rays scattered by different targets. The device has a $600-\mu m-$thick carbon fiber window with a crystal volume of 250 cm^3 and yields very efficient photon detection. The pre-amplifier is located outside the shield-detector system for stable and noise-free measurements. The detector is placed inside an ultra-low-background 15-cm-thick lead shield (Canberra Model 777-1). The shield is covered with a 2-mm copper sheet to absorb X-rays from lead in the energy range 75–85 keV. The instrumental resolution is determined using multiple calibration sources of ^{210}Pb, ^{241}Am, ^{57}Co, ^{137}Cs and ^{54}Mn, with photopeaks at 46.5, 59.5, 122.1, 136.5, 661.6 and 834.8 keV, respectively. The function is obtained by fitting these peaks to a Gaussian curve. For the particular case of 206.1 keV (the Compton peak), the full width at half-maximum (FWHM) is 0.9 keV.

Four lead plates (4.5 cm thick) with identical holes ($\phi=0.5$ cm) are used as collimators. All measurements are performed at 135°. The geometric divergence of the incident beam slits is $\pm3°$. The distance between the source and the sample is 42.43 ± 0.1 cm and the distance between the sample and the detector is 40 ± 0.1 cm. The instrumental resolution is estimated as 0.48 a.u. The absolute detector efficiency at the energy corresponding to the Compton peak (206.1 keV) at a sample-detector distance of 40 cm is 4.91×10^{-5}. Detector output spectra are acquired using commercial software [59] and are preset at 8192 channels using a digital spectrum analyzer (DSA2000). All of the subsystems required for high-quality spectral acquisition are integrated into a single physical unit, including a high-voltage power supply, a digital stabilizer, MCA memory and an Ethernet network interface.

Double-scattering corrections at the Compton peak are taken into account following a similar procedure to that described by Fajardo et al. [60]. These corrections include analytical calculations and Monte Carlo simulations [61]. Sample absorption corrections are included using a relative absorption factor [3]. In our experimental set-up, the incident photon energy is 661.66 keV and the incoming photon angle is 45°. In this case, the linear attenuation coefficients, determined experimentally via a narrow beam attenuation measurement, are 0.1282, 0.2045, and 0.3179 cm^{-1} for Be, Al, and Ti, respectively. Similarly, for the Compton peak at 206.1 keV and 0°, the linear attenuation coefficients are 0.2016, 0.3269, and 0.5953 cm^{-1}. Finally, the Compton peaks are corrected with an absorption factor of 1.098, 1.031 and 1.016 for Be, Al and Ti, respectively.

The source is located outside the shielding-detector system, so air scattering is negligible. However, background radiation from vacuum chamber scattering is subtracted from the Compton peak. As an illustration of the importance of this radiation, Fig. 1 shows the background intensity compared to the Compton scattering spectrum using raw energy data for a 0.3-mm-thick Ti sample. The Compton peak centered at channel number 2333 corresponds to energy of 206.1 keV and the area under the peak comprises 200,000 counts. It is clear that the background corresponds to approximately 10% of the CP intensity.

Once the background radiation is subtracted from the Compton spectrum, double scattering and the absorption factor should be included in the correction. Finally, the spectrum is deconvoluted according to the instrumental response function. This deconvolution involves fast Fourier transforms applied by commercial software [62]. The resulting curve is transformed from energy to momentum transfer q to determine $J(q)$ according to Eq. (3). Finally, the normalization $\int J(q)\,dq=Z/2$, where Z is the atomic number of the element under study, is applied.

4. Results

To obtain theoretical results, we developed a FORTRAN code to calculate CPs, starting from tabulated radial wavefunctions obtained from several atomic structure programs. We calculated CPs using electron orbitals obtained from GGA-PBE functionals. We made a number of assumptions and set some parameters to calculate the bulk structure using the OpenMX code. In some cases the parameters are physical properties of the elements and in others they are chosen as a tradeoff between computational accuracy and efficiency. The OpenMX webpage [51] presents a series of recommended input files for different atomic basis orbitals. These orbitals are the product of a systematic study and a comprehensive investigation of convergence properties for a wide range of elements [52,53]. We tested these recommended parameters and used them, with minor modifications, in our calculations.

For comparison, theoretical results obtained using atomic HF wavefunctions calculated using computer codes described by Fischer [64] are presented. We also compare our findings to other experimental and theoretical results. Fermi momenta were calculated using the reciprocal function and second derivatives of the CPs.

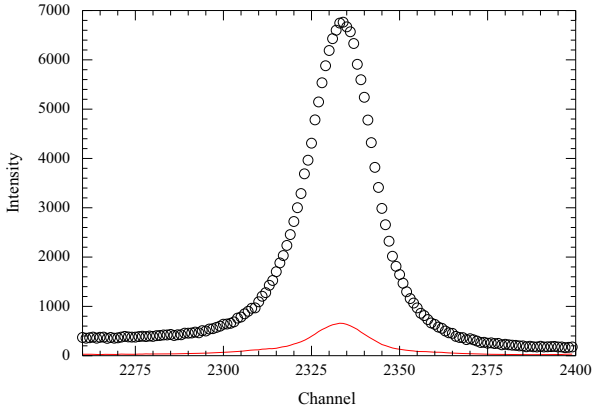

Fig. 1. Energy spectrum (circles, raw data) for a Ti sample of 0.3 mm in thickness. The solid line denotes the background intensity.

4.1. Beryllium

The ground state of Be is $1s^2 2s^2$, among which the 2s electrons are considered as valence electrons. We assumed that the solid bulk has a face-centered cubic (fcc) structure with a lattice constant of 3.158 Å. Atomic radial wavefunctions were calculated up to a cutoff radius of 7.0 Å.

Comparisons between DFT and free-atom HF reduced wavefunctions are shown in Fig. 2. The latter were obtained using the HF package described by Fischer [64]. It is evident that the radial reduced wavefunctions for the inner electrons (P_{1s}) are very similar for both theories. However, the CPs for valence electrons clearly reflect the fact that the free-atom HF does not take into account any effect concerning the metallic structure (Fig. 3).

The GGA-PBE theoretical results for the Be CP are presented in Table 1, where $J_{1s}(q)$ is the CP for internal electron orbitals and $J_{2s}(q)$ is the CP for valence electrons. The total CP is $J(q)_{\mathrm{tot}} = J_{1s}(q) + J_{2s}(q)$ and $J(q)_{\mathrm{exp}}$ denotes the experimental results.

The theoretical total (core plus valence) CP for Be is shown in Fig. 4. Our experimental and theoretical results are compared in terms of the difference $\Delta J(q) \equiv J^{\mathrm{exp}} - J^{\mathrm{th}}$. We also compare our experimental results with those obtained by Manninen and Suortti [34]. A value for the Fermi momentum can be extracted from the CP curve in different ways. Roughly, it is the momentum transfer value corresponding to the greatest decrease in CP slope for valence electrons. It is possible to overcome poor resolution by performing a one-dimensional Fourier transform of the CP. For simple metallic systems this yields information about the Fermi momentum p_F by searching for zero values of the autocorrelation function [65]:

$$B(z) = \sqrt{\frac{1}{2\pi}} \int_{-\infty}^{\infty} J(q) \exp(-iqz)\, dq. \tag{8}$$

For a free-electron CP, the first zero for $B(z)$ is located at a z value for which $p_F z = 4.493$. Fig. 5 shows the reciprocal $B(z)$ function for Be, calculated by Fourier transformation of both theoretical and experimental CPs. For theoretical CP values for Be, the $B(z)$ function intersects the horizontal axis at $z = 4.6$ a.u., so $p_F = 0.98$ a.u. An alternative way to estimate the Fermi momentum is through CP derivatives. The second derivative d^2J/dq^2 generally peaks at a position corresponding to the principal Fermi surface radius, as shown in Fig. 5 for Be. The second derivative of the theoretical CP peaks at a value slightly greater than $q = 1$ a.u., which is quite similar to the Fermi momentum value estimated using the $B(z)$ function. The second derivative of the experimental CP leads to a higher value of $q = 1.1$ a.u. However, the number of data points is insufficient for an accurate numerical derivative. Therefore, both the first and second derivatives of the CP show considerable noise. To reduce this noise, we applied a spline interpolation of the data points, the corresponding derivative, and a further Gaussian convolution. The results are in reasonably good agreement with the Fermi momentum reported by Chou et al. of $p_F = 1.03$ a.u. [33].

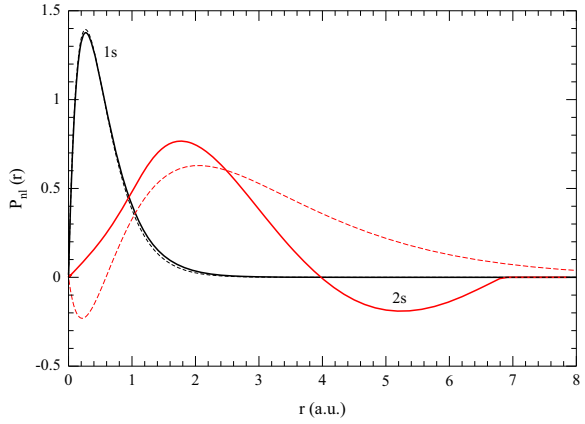

Fig. 2. Radial reduced wavefunctions ($P_{nl}(r) = r\, R_{nl}(r)$) for Be calculated using DFT (solid curves) and the free-atom HF method (dashed curves).

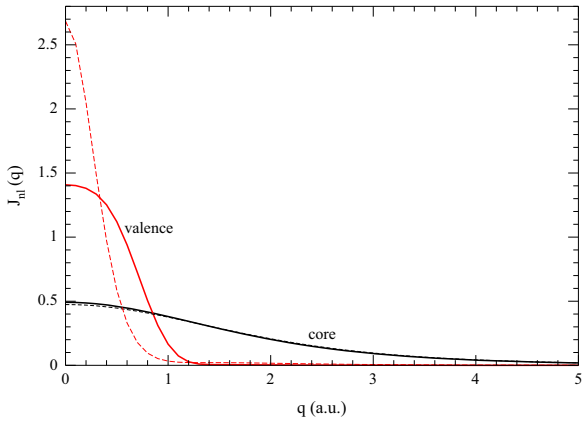

Fig. 3. Compton profiles for Be calculated using DFT (solid curves) and free-atom HF wavefunctions (dashed curves).

Table 1
Compton profiles for Be.

q (a.u.)	$J_{1s}(q)$	$J_{2s}(q)$	$J(q)_{\mathrm{tot}}$	$J(q)_{\mathrm{exp}}$	q (a.u.)	$J_{1s}(q)$	$J_{2s}(q)$	$J(q)_{\mathrm{tot}}$	$J(q)_{\mathrm{exp}}$
0	4.916E−1	1.408E+0	1.899E+0	1.888E+0	1.7	2.507E−1	4.515E−3	2.552E−1	2.571E−1
0.1	4.903E−1	1.402E+0	1.892E+0	1.873E+0	1.8	2.338E−1	4.063E−3	2.378E−1	2.394E−1
0.2	4.863E−1	1.380E+0	1.866E+0	1.826E+0	1.9	2.176E−1	3.764E−3	2.213E−1	2.208E−1
0.3	4.798E−1	1.335E+0	1.815E+0	1.754E+0	2.0	2.022E−1	3.575E−3	2.057E−1	2.032E−1
0.4	4.710E−1	1.252E+0	1.723E+0	1.653E+0	2.2	1.738E−1	3.157E−3	1.770E−1	1.751E−1
0.5	4.599E−1	1.120E+0	1.580E+0	1.522E+0	2.4	1.488E−1	2.253E−3	1.510E−1	1.479E−1
0.6	4.469E−1	9.398E−1	1.386E+0	1.367E+0	2.6	1.269E−1	1.144E−3	1.281E−1	1.258E−1
0.7	4.322E−1	7.251E−1	1.157E+0	1.201E+0	2.8	1.080E−1	5.368E−4	1.086E−1	1.073E−1
0.8	4.161E−1	5.048E−1	9.209E−1	1.001E+0	3.0	9.184E−2	3.454E−4	9.219E−2	9.16E−2
0.9	3.988E−1	3.107E−1	7.095E−1	7.866E−1	3.5	6.108E−2	6.852E−5	6.115E−2	6.07E−2
1.0	3.807E−1	1.651E−1	5.458E−1	5.635E−1	4.0	4.077E−2	1.917E−5	4.078E−2	4.04E−2
1.1	3.621E−1	7.378E−2	4.358E−1	4.177E−1	4.5	2.744E−2	1.633E−5	2.746E−2	2.72E−2
1.2	3.431E−1	2.752E−2	3.706E−1	3.694E−1	5.0	1.868E−2	1.007E−5	1.872E−2	1.85E−2
1.3	3.240E−1	9.828E−3	3.339E−1	3.353E−1	6.0	9.007E−3	1.941E−6	9.009E−3	8.94E−3
1.4	3.051E−1	5.483E−3	3.106E−1	3.120E−1	7.0	4.580E−3	1.104E−6	4.581E−3	4.57E−3
1.5	2.865E−1	5.099E−3	2.916E−1	2.933E−1	8.0	2.449E−3	7.276E−7	2.450E−3	2.46E−3
1.6	2.683E−1	4.962E−3	2.733E−1	2.709E−1	9.0	1.371E−3	3.319E−7	1.371E−3	1.38E−3

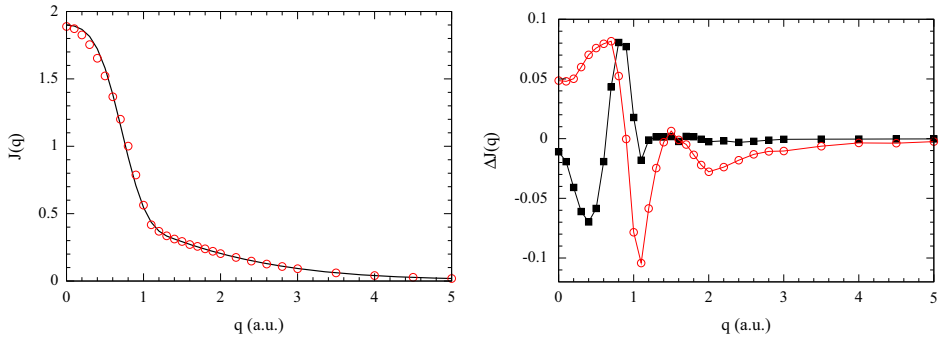

Fig. 4. Left: Total Compton profile for Be calculated using DFT (solid curves). Experimental results are denoted by circles. Circle size corresponds to the experimental error limits. Right: Comparison of our experimental Compton profiles for Be and our theoretical calculations and other experimental results. Solid squares denote the difference $\Delta J(q) \equiv J^{exp} - J^{th}$ between experimental measurements and GGA-PBE theoretical calculations. Empty circles denote differences between our experimental results and those reported by Manninen and Suortti [34].

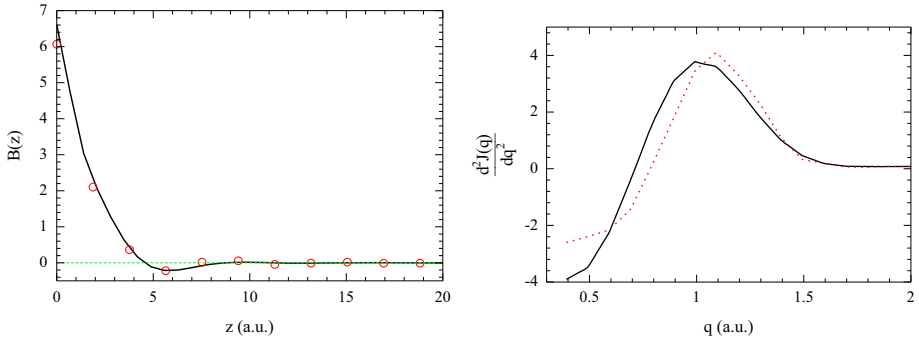

Fig. 5. Left: Autocorrelation function $B(z)$ for Be. The solid curve is the Fourier transform of the theoretical values. Circles denote the reciprocal function for experimental data. Right: Second derivative of the Compton profile for theoretical (solid curve) and experimental data (dashed curve).

4.2. Aluminum

The Al solid bulk is represented as a face-centered cubic (fcc) structure. We assumed $a=4.028$ Å and a radial cutoff of 7.0 Å. The $3s^2$ and 3p electrons were considered as valence electrons.

DFT and HF wavefunction results for Al are shown in Fig. 6. The core radial P_{1s}, P_{2s} and P_{2p} wavefunctions are very similar for the DFT and HF methods. By contrast, the P_{3s} and P_{3p} valence orbitals differ significantly for the two approaches. The DFT theoretical CP results for Al are presented in Table 2, where $J(q)_{core} = J_{1s}(q) + J_{2s}(q) + J_{2p}(q)$ and $J(q)_{val} = J_{3s}(q) + J_{3p}(q)$.

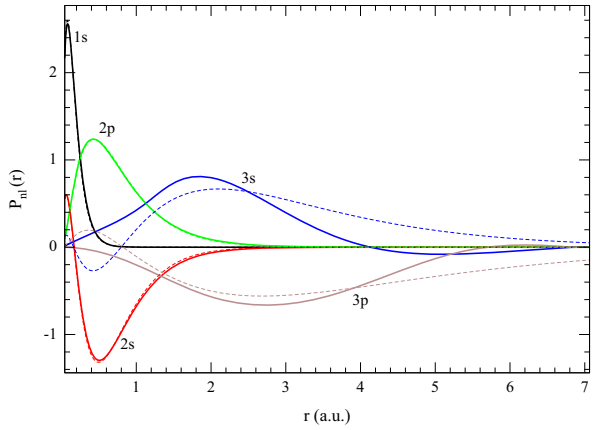

Fig. 6. Radial reduced wavefunctions for Al calculated using DFT (solid curves) and the free-atom HF method (dashed curves).

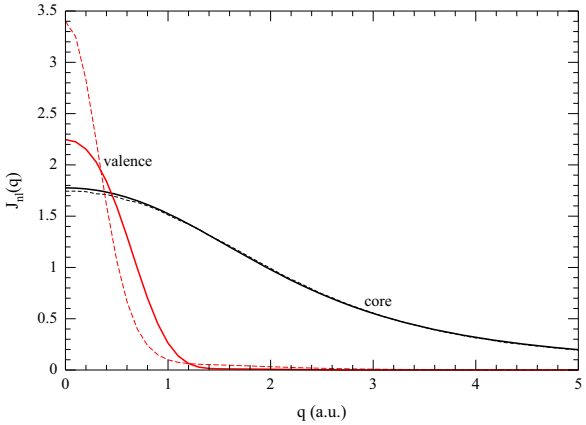

Fig. 7. Compton profile for Al calculated using DFT (solid curves) and free-atom HF wavefunctions (dashed curves).

The Al CPs are displayed in Fig. 7 and the theoretical and experimental total CPs in Fig. 8. The difference between our experimental and theoretical results is less than 5% for the whole data range. The difference between our experimental results and those obtained by Halonen et al. [66] is approximately 5% and less than 10% over the whole q range. Our results are in better agreement with those of Ahuja and Sharma [39] and the maximum discrepancy (at the origin) is less than 3%. The Fermi momentum was calculated using the two methods described above. The first zero passage of the reciprocal function $B(z)$ is located at $z=4.87$, which corresponds to $p_F=0.92$ a.u. The second derivative has a maximum at $q=0.99$ a.u. The result reported by Das and Chaddah [67] is $p_F=0.926$ a.u.

Table 2
Compton profiles for Al.

q (a.u.)	$J_{core}(q)$	$J_{val}(q)$	$J(q)_{tot}$	$J(q)_{exp}$	q (a.u.)	$J_{core}(q)$	$J_{val}(q)$	$J(q)_{tot}$	$J(q)_{exp}$
0	1.776E+0	2.247E+0	4.023E+0	3.936E+0	1.7	1.144E+0	1.072E−2	1.155E+0	1.184E+0
0.1	1.773E+0	2.224E+0	3.998E+0	3.877E+0	1.8	1.087E+0	9.755E−3	1.098E+0	1.135E+0
0.2	1.765E+0	2.154E+0	3.920E+0	3.798E+0	1.9	1.032E+0	8.483E−3	1.041E+0	1.072E+0
0.3	1.753E+0	2.027E+0	3.780E+0	3.649E+0	2.0	9.789E−1	7.350E−3	9.862E−1	1.022E+0
0.4	1.734E+0	1.840E+0	3.575E+0	3.452E+0	2.2	8.764E−1	4.633E−3	8.811E−1	9.012E−1
0.5	1.711E+0	1.593E+0	3.305E+0	3.175E+0	2.4	7.821E−1	2.608E−3	7.847E−1	8.051E−1
0.6	1.683E+0	1.303E+0	2.986E+0	2.908E+0	2.6	6.965E−1	1.245E−3	6.978E−1	7.136E−1
0.7	1.649E+0	9.950E−1	2.645E+0	2.612E+0	2.8	6.199E−1	5.362E−4	6.205E−1	6.272E−1
0.8	1.612E+0	7.017E−1	2.314E+0	2.314E+0	3.0	5.520E−1	2.621E−4	5.523E−1	5.580E−1
0.9	1.570E+0	4.515E−1	2.022E+0	1.982E+0	3.5	4.160E−1	1.362E−4	4.161E−1	4.284E−1
1.0	1.524E+0	2.618E−1	1.786E+0	1.820E+0	4.0	3.186E−1	1.120E−4	3.187E−1	3.241E−1
1.1	1.475E+0	1.358E−1	1.611E+0	1.649E+0	4.5	2.487E−1	6.419E−5	2.488E−1	2.545E−1
1.2	1.423E+0	6.284E−2	1.487E+0	1.538E+0	5.0	1.981E−1	1.957E−5	1.980E−1	1.97E−1
1.3	1.369E+0	2.806E−2	1.398E+0	1.444E+0	6.0	1.317E−1	3.211E−6	1.317E−1	1.35E−1
1.4	1.314E+0	1.502E−2	1.329E+0	1.377E+0	7.0	9.178E−2	2.029E−6	9.178E−2	9.6E−2
1.5	1.257E+0	1.168E−2	1.269E+0	1.299E+0	8.0	6.577E−2	3.305E−7	6.577E−2	7.1E−2
1.6	1.200E+0	1.117E−2	1.211E+0	1.247E+0	9.0	4.782E−2	1.875E−7	4.782E−2	5.6E−2

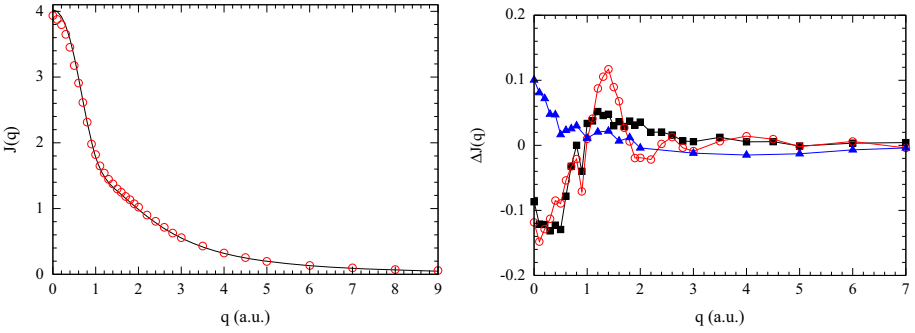

Fig. 8. Left: Total Compton profile for Al calculated using DFT (solid curves). Experimental results are shown by circles and circle size denotes the experimental error limit. Right: Comparison of our experimental Compton profiles for Al to our theoretical calculations and other experimental results. Solid squares denote the difference $\Delta J(q) \equiv J^{exp} - J^{th}$ between experimental measurements and GGA-PBE theoretical calculations. Empty circles show differences between our experimental results and those reported by Halonen et al. [66]. Solid triangles show differences between our experiments and those of Ahuja and Sharma [39].

4.3. Titanium

The Ti solid bulk is considered as a face-centered cubic (fcc) structure and we assumed $a=4.10$ Å and a radial cutoff of 7.0 Å. The DFT and HF wavefunctions are compared in Fig. 9, where 1s, 2s, 2p, 3s and 3p are the core orbitals. The valence orbitals are 3d and 4s. The DFT theoretical CP results for Ti are presented in Table 3, where $J(q)_{core} = J_{1s}(q) + J_{2s}(q) + J_{2p}(q) + J_{3s}(q) + J_{3p}(q)$ and $J(q)_{val} = J_{3d}(q) + J_{4s}(q)$.

The CPs for Ti are displayed in Fig. 10 and the theoretical and experimental total CPs in Fig. 11. In contrast to the Be and Al cases, for which the CP slope changes discontinuously at the Fermi momentum, it is hard to estimate a slope value from the smooth CP curve for Ti. We cannot use either of the methods described above to calculate the Fermi momentum. The autocorrelation function $B(z)$ decreases too abruptly and does not show any negative autocorrelation. The second derivative of the CP has peaks at $q=0.67$ and at $q=1.7$. These values differ significantly from the value of $p_F = 1.08 \pm 0.04$ a.u. measured by Weiss [68].

In general, the ground state commonly assumed for metallic Ti is $3d^2\ 4s^2$, which corresponds to the free-atom Ti case. This assumption was made for CP RFA calculations by Felsteiner and Pattison [69] and free-electron gas model calculations by Lasser et al. [70] and Weiss [71], for example. However, for our calculations we assume a ground state of $3d^3$ 4 s for metallic Ti, in accordance with Berggren et al. [41], Moruzzi et al. [17], and Raj et al. [72]. For comparison, CP results

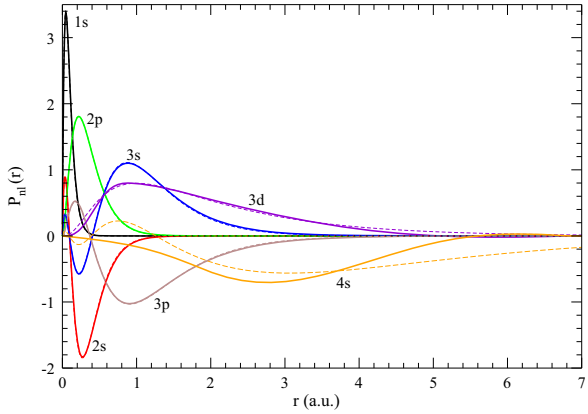

Fig. 9. Radial reduced wavefunctions for Ti, calculated by using DFT (solid curves) and free-atom HF method (dashed curves).

obtained assuming a $3d^2\ 4s^2$ configuration for the ground state are plotted in Fig. 11. There is a notable discrepancy for both our experimental values and our GGA-PBE calculations at low momentum transfer values. Our theoretical and experimental values are also compared in Fig. 11. There is a peak in the discrepancy curve at $q=0.6$ a.u., where the difference is approximately 7%. Comparison of our experimental results to those reported by Felsteiner and Pattison [69] reveals a difference of less than 2%.

Table 3
Compton profiles for Ti.

q (a.u.)	$J_{core}(q)$	$J_{val}(q)$	$J(q)_{tot}$	$J(q)_{exp}$	q (a.u.)	$J_{core}(q)$	$J_{val}(q)$	$J(q)_{tot}$	$J(q)_{exp}$
0	3.474E+0	1.961E+0	5.435E+0	5.506E+0	1.7	1.592E+0	3.597E−1	1.952E+0	1.907E+0
0.1	3.465E+0	1.914E+0	5.380E+0	5.433E+0	1.8	0.479E+0	3.209E−1	1.799E+0	1.769E+0
0.2	3.439E+0	1.785E+0	5.225E+0	5.336E+0	1.9	1.376E+0	2.877E−1	1.664E+0	1.651E+0
0.3	3.396E+0	1.599E+0	4.996E+0	5.176E+0	2.0	1.284E+0	2.587E−1	1.543E+0	1.533E+0
0.4	3.332E+0	1.391E+0	4.724E+0	4.996E+0	2.2	1.127E+0	2.099E−1	1.337E+0	1.346E+0
0.5	3.253E+0	1.194E+0	4.447E+0	4.740E+0	2.4	1.002E+0	1.697E−1	1.172E+0	1.181E+0
0.6	3.153E+0	1.032E+0	4.184E+0	4.482E+0	2.6	9.028E+0	1.370E−1	1.0640E+0	1.056E+0
0.7	3.035E+0	9.128E−1	3.948E+0	4.170E+0	2.8	8.237E−1	1.110E−1	9.347E−1	9.515E−1
0.8	2.903E+0	8.332E−1	3.737E+0	3.881E+0	3.0	7.597E−1	9.031E−2	8.500E−1	8.709E−1
0.9	2.759E+0	7.794E−1	3.539E+0	3.553E+0	3.5	6.413E+0	5.379E−2	6.951E−1	7.050E−1
1.0	2.607E+0	7.356E−1	3.343E+0	3.292E+0	4.0	5.547E−1	3.214E−2	5.869E−1	5.860E−1
1.1	2.451E+0	6.899E−1	3.141E+0	3.044E+0	4.5	4.829E−1	1.907E−2	5.019E−1	4.800E−1
1.2	2.294E+0	6.371E−1	2.931E+0	2.843E+0	5.0	4.197E−1	1.125E−2	4.309E−1	4.100E−1
1.3	2.139E+0	5.779E−1	2.717E+0	2.610E+0	6.0	3.135E−1	3.690E−3	3.172E−1	3.175E−1
1.4	1.990E+0	5.165E−1	2.506E+0	2.398E+0	7.0	2.323E−1	1.046E−3	2.333E−1	2.435E−1
1.5	1.848E+0	4.579E−1	2.306E+0	2.195E+0	8.0	1.720E−1	2.387E−4	1.723E−1	2.050E−1
1.6	1.715E+0	4.052E−1	2.120E+0	2.034E+0	9.0	1.280E−1	5.231E−5	1.281E−1	1.720E−1

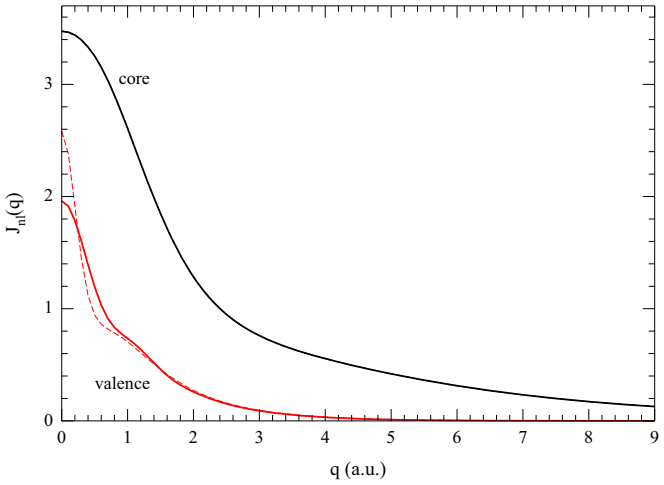

Fig. 10. Compton profile for Ti calculated using DFT (solid curves) and free-atom HF wavefunctions (dashed curves).

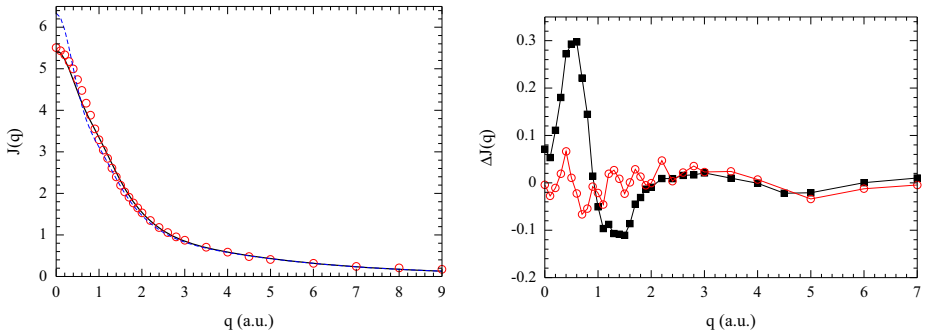

Fig. 11. Left: Total Compton profile for Ti calculated using DFT (solid curves) and assuming a $3d^3$ 4 s configuration for the ground state. Experimental results are shown by circles and circle size indicates the experimental error limit. For comparison, the dashed lines represent total CP results calculated assuming a $3d^2$ $4s^2$ configuration for the ground state. Right: Comparison of our experimental Compton profiles for Ti and our theoretical calculations and other experimental results. Solid squares denote the difference $\Delta J(q) \equiv J^{exp} - J^{th}$ between experimental measurements and GGA-PBE theoretical calculations. Empty circles show differences between our experimental results and those of Felsteiner and Pattison [69].

5. Conclusions

CP measurement provides a good tool for verifying DFT quality. We presented experimental and theoretical results for isotropic CPs for Be, Al and Ti and tabulated electron momentum transfer values from $q=0$–9 a.u.

The similarity of our experimental CPs to other measurements demonstrates that our spectrometer and the numerical methods used for data analysis provide fairly accurate values. The agreement between our GGA calculations and experimental results is satisfactory for a wide range of q values.

Wavefunctions for the core orbitals of Be, Al and Ti are hardly affected by the crystalline potential, as indicated by the agreement between HF and DFT calculations. By contrast, valence electrons require a more sophisticated theory for a realistic description of the electronic properties in solids.

CP experiments and GGA calculations for Be and Al depart slightly around $q=0$ and near the Fermi momentum. However, comparisons between GGA-PBE and other DFT calculations show that GGA-PBE provides results with the same order of accuracy as the local density approximation plus additional corrections (e.g., Lam–Platzman correction). If higher accuracy is required, a theoretical procedure that includes virtual promotions produced by correlation effects [73,74] must be developed. This issue is under investigation.

It is widely assumed that the ground-state configuration of metallic Ti is the same as the free-atom configuration. However, we obtained better agreement with the experimental CP results when the configuration assumed for the Ti ground state was $3d^3$ 4s rather than $3d^2$ $4s^2$.

Acknowledgments

We are grateful to Jorge Fernandez for valuable help in installing the programs used and for support received from Universidad Nacional del Centro de la Provincia de Buenos Aires (UNCPBA, Argentina). We also thank Professor B. Ahuja for kindly providing us his experimental results. D.M. acknowledges support by UBACyT 239 from Universidad de Buenos Aires and PIP 200901/552 from CONICET.

References

[1] B.G. Williams (Ed.), Compton Scattering, McGraw-Hill, New York, 1977.
[2] M.J. Cooper, Rep. Prog. Phys. 48 (1985) 415.
[3] M.J. Cooper (Ed.), X-Ray Compton Scattering, Oxford University Press, New York, 2004.
[4] F. Biggs, L.B. Mendelsohn, J.B. Mann, Atom. Data Nucl. Data Tables 16 (1975) 201.
[5] P. Eisenberger, P.M. Platzman, Phys. Rev. A 2 (1970) 415.
[6] P. Eisenberger, W.A. Reed, Phys. Rev. A 5 (1972) 2085.
[7] P. Holm, R. Ribberfors, Phys. Rev. A 40 (1989) 6251.
[8] P. Jaiswal, A. Shukla, Phys. Rev. A 75 (2007) 022504.
[9] H. Sakurai, H. Ota, N. Tsuji, M. Itou, Y. Sakurai, J. Phys. B 44 (2011) 065001.
[10] A.J. Thakkar, Adv. Chem. Phys. 128 (2004) 303.
[11] J.R. Hart, A.J. Thakkar, Int. J. Quantum Chem. 102 (2005) 673.
[12] A. Erba, C. Pisani, S. Casassa, L. Maschio, M. Schütz, D. Usvyat, Phys. Rev. B 81 (2010) 165108.
[13] C. Pisani, A. Erba, S. Casassa, M. Itou, Y. Sakurai, Phys. Rev. B 84 (2011) 245102.
[14] C. Pisani, M. Itou, Y. Sakurai, R. Yamaki, M. Ito, A. Erba, L. Maschio, Phys. Chem. Chem. Phys. 13 (2011) 933.
[15] A. Erba, M. Itou, Y. Sakurai, R. Yamaki, M. Ito, S. Casassa, L. Maschio, A. Terentjevs, C. Pisani, Phys. Rev. B 83 (2011) 125208.
[16] R.O. Jones, O. Gunnarsson, Rev. Mod. Phys. 61 (1989) 689.
[17] V.L. Moruzzi, J.F. Janak, A.R. Williams, Calculated Electronic Properties of Metals, Pergamon Press, 1978.
[18] L. Lam, P. Platzman, Phys. Rev. B 9 (1974) 5122.
[19] D.A. Cardwell, M.J. Cooper, J. Phys. Condens. Matter 1 (1989) 9357.
[20] B. Barbiellini, A. Bansil, J. Phys. Chem. Solids 62 (2001) 2181.
[21] J.P. Perdew, K. Burke, M. Ernzerhof, Phys. Rev. Lett. 77 (1996) 3865.
[22] N. Moll, M. Bockstedte, M. Fucks, E. Pehlke, M. Scheffler, Phys. Rev. B 52 (1995) 2550.
[23] A. Dal Corso, A. Pasquarello, A. Baldereschi, R. Car, Phys. Rev. B 53 (1996) 1180.
[24] V.N. Staroverov, G.E. Scuseria, J. Tao, J.P. Perdew, Phys. Rev. B 69 (2004) 075102.
[25] M.A.G. Dixon, J.A. Duffy, S. Gardelis, J.E. McCarthy, M.J. Cooper, S.B. Dugdale, T. Jarlborg, D.N. Timms, J. Phys. Condens. Matter 10 (1998) 2759.
[26] T. Baruah, R. Zope, A. Kshirsagar, Phys. Rev. B 60 (1999) 10770.
[27] R.R. Zope, Phys. Rev. A 62 (2000) 064501.
[28] B.L. Ahuja, N.L. Heda, Pramana J. Phys. 68 (2007) 843.
[29] W.C. Phillip, R.J. Weiss, Phys. Rev. 171 (1968) 790.
[30] G. Loupias, J. Petiau, A. Issolah, M. Schneider, Phys. Status Solidi B 102 (1980) 79.
[31] R. Currat, P.D. DeCicco, R. Kaplow, Phys. Rev. B 3 (1971) 243.
[32] M. Chou, P. Lam, M. Cohen, Phys. Rev. Lett. 49 (1982) 1452.
[33] M. Chou, P. Lam, M. Cohen, Phys. Rev. B 28 (1983) 1696.
[34] S. Manninen, P. Suortti, Philos. Mag. B 40 (1979) 199.
[35] J. Aguiar, H. Di Rocco, A. Arazi, Physica B 406 (2011) 354.
[36] M. Cooper, P. Pattison, B. Williams, K. Pandey, Philos. Mag. 29 (1974) 1237.
[37] G. Sohoni, D. Kanhere, Solid State Commun. 48 (1983) 619.
[38] T. Ohata, M. Itou, I. Matsumoto, Y. Sakurai, H. Kawata, N. Shiotani, S. Kaprzyk, P. E. Mijnarends, A. Bansil, Phys. Rev. B 62 (2000) 16528.
[39] B.L. Ahuja, M. Sharma Pramana, J. Phys. 65 (2005) 137.
[40] K.F. Berggren, in: B.G. Williams (Ed.), Compton Scattering, McGraw-Hill, New York, 1977, Chapter IV.
[41] K.F. Berggren, S. Manninen, T. Paakkari, Phys. Rev. B 8 (1973) 2516.
[42] S. Manninen, T. Paakkari, J. Phys. C 9 (1976) 95.
[43] N. Bacalis, N. Papanicolaou, D. Papaconstantopoulos, J. Phys. F Met. Phys. 16 (1986) 1471.
[44] G. Sharma, K. Joshi, M. Dhaka, M. Mishra, R. Kothari, B. Sharma, Intermetallics 19 (2011) 1107.
[45] P. Kaijser, V.H. Smith, Adv. Quantum Chem. 10 (1977) 37.
[46] P. Hohenberg, W. Kohn, Phys. Rev. 136 (1964) B864.
[47] W. Kohn, L.S. Sham, Phys. Rev. 140 (1965) A1133.
[48] W. Kohn, Rev. Mod. Phys. 71 (1998) 1253.
[49] ⟨http://www.openmx-square.org/adpack_man2.2⟩.
[50] N. Troullier, J.L. Martins, Phys. Rev. B 43 (1991) 1993.
[51] ⟨http://www.openmx-square.org/⟩.
[52] T. Ozaki, Phys. Rev. B 67 (2003) 155108.
[53] T. Ozaki, H. Kino, Phys. Rev. B 69 (2004) 195113.
[54] M. Toyoda, T. Ozaki, Phys. Rev. A 83 (2011) 032515.
[55] T. Ozaki, M. Toyoda, Comput. Phys. Commun. 182 (2011) 1245.
[56] F. Bell, J. Chem. Phys. 85 (1986) 303.
[57] I.G. Kaplan, B. Barbiellini, A. Bansil, Phys. Rev. B 68 (2003) 235104.
[58] R.H. Pratt, L.A. Lajohn, T. Suric, B.K. Chatterjee, S.C. Roy, Nucl. Instrum. Methods B 261 (2007) 175.
[59] Genie 2000, Canberra Industries, Meriden, CT, USA.
[60] P. Fajardo, V. Honkimäki, T. Buslaps, P. Sourtti, Nucl. Instrum. Methods B 134 (1998) 337.
[61] ⟨http://shape.ing.unibo.it/html/mcshape.html⟩.
[62] ORIGIN-PRO 8 Lab-data analysis (Origin Corporation), Northampton, (01060) MA, USA.
[64] C.F. Fischer, Comp. Phys. Commun. 64 (1991) 369.
[65] P. Pattison, B. Williams, Solid State Commun. 20 (1976) 585.
[66] V. Halonen, B.G. Williams, T. Paakkari, Phys. Fenn. 10 (1975) 107.
[67] G.P. Das, P. Chaddah, Solid State Commun. 45 (1983) 607.
[68] R.J. Weiss, Philos. Mag. 25 (1972) 1511.
[69] J. Felsteiner, P. Pattison, Phys. Rev. B 13 (1976) 2702.
[70] R. Lasser, B. Lengeler, G. Arnold, Phys. Rev. B 22 (1980) 663.
[71] R.J. Weiss, Phys. Rev. Lett. 24 (1970) 883.
[72] S. Raj, H.C. Padhi, P. Palit, D.K. Basa, M. Polasik, F. Pawlowski, Phys. Rev. B 65 (2002) 193105.
[73] B. Barbiellini, M.J. Puska, T. Torsti, R.M. Nieminen, Phys. Rev. B 51 (1995) 7341.
[74] J. Kwiatkowska, B. Barbiellini, S. Kaprzyk, A. Bansil, H. Kawata, N. Shiotani, Phys. Rev. Lett. 96 (2006) 186403.